RSC Advances

PAPER

View Article Online
View Journal | View Issue

Cite this: *RSC Adv.*, 2019, **9**, 19253

Facile *in situ* growth of ZnO nanosheets standing on Ni foam as binder-free anodes for lithium ion batteries†

Tianlai Xia,[ac] Yingqian Wang,[ac] Chengkang Mai,[ac] Guangxing Pan,[ac] Ling Zhang,[*b] Weiwei Zhao[ac] and Jiaheng Zhang[*acd]

Received 6th May 2019
Accepted 31st May 2019

DOI: 10.1039/c9ra03373d

rsc.li/rsc-advances

ZnO has attracted increasing attention as an anode for lithium ion batteries. However, the application of such anode materials remains restricted by their poor conductivity and large volume changes during the charge/discharge process. Herein, we report a simple hydrothermal method to synthesize ZnO nanosheets with a large surface area standing on a Ni foam framework, which is applied as a binder-free anode for lithium ion batteries. ZnO nanosheets were grown *in situ* on Ni foam, resulting in enhanced conductivity and enough space to buffer the volume changes of the battery. The ZnO nanosheets@Ni foam anode showed a high specific capacity (1507 mA h g^{-1} at 0.2 A g^{-1}), good capacity retention (1292 mA h g^{-1} after 45 cycles), and superior rate capacity, which are better than those of ZnO nanomaterial-based anodes reported previously. Moreover, other transition metal oxides, such as Fe_2O_3 and NiO were also formed *in situ* on Ni foam with perfect standing nanosheets structures by this hydrothermal method, confirming the universality and efficiency of this synthetic route.

Introduction

Lithium ion batteries (LIBs) play crucial roles in energy storage and are employed in portable electronic devices and electric vehicles.[1–3] With the development of electronic technology, the components were highly integrated to obtain devices with small volume and high power output.[4–6] Conventional commercial graphite anode materials (372 mA h g^{-1}) cannot meet the demand of normal battery usage in daily life.[7] Thus, transition metal oxides (TMOs) are used as promising anode materials due to their high specific capacity, which is several times higher than that of graphite.[8–11] Among various TMOs, ZnO is the most common material applied in electronic devices, such as solar cells, light emitting diodes, sensors, and photodetectors due to its superior electrochemical performance, non-toxicity, facile preparation, and low cost.[12–19] Meanwhile, ZnO has attracted much attention as an alternative anode material of LIBs with a high theoretical capacity of 978 mA h g^{-1}.[20–23]

Nevertheless, ZnO is restricted by its large volume change (221%)[24,25] and poor conductivity during the charge and discharge process of LIBs, leading to the low capacity, rapid capacity fade upon cycling, and weak rate capacity. To address these issues, various studies have been attempted to regulate the structures of ZnO to enhance its conductivity and stability, such as adjusting the morphology,[20,21] coating and encapsulating the surface,[26–29] and functionalizing with other materials.[30–35] The rational designed strategy of nanostructures and composites relieved the large volume changes to slow the electrode disintegrations.

However, these methods cannot improve the conductivity of ZnO anode effectively because of the present macroscopic gap. Recently, atomic layer deposition and electrospinning methods have been used to 'deposit' ZnO uniformly on the surface of good conductors directly to remove the macroscopic gap between ZnO and the conductor and reduce the interface resistance largely.[36–38] However, the structures of ZnO cannot be optimized by atomic layer deposition or electrospinning techniques, and the specific capacity of LIBs was still low and rapidly faded. Furthermore, the two techniques are too expensive for practical applications.

Herein, we report a facile hydrothermal method to synthesize ZnO nanosheets standing on Ni foam as a binder-free anode for LIBs. ZnO nanosheets were *in situ* grown uniformly on Ni foam framework, which exposed with large surface area, good conductivity, and large buffer space, enhancing the electrochemical performance of LIBs remarkably. Tested as the anode, ZnO nanosheets@Ni foam delivered a high specific

[a]State Key Laboratory of Advanced Welding and Joining, Harbin Institute of Technology, Shenzhen, 518055, China. E-mail: jiahengzhang@hit.edu.cn
[b]School of Science, Harbin Institute of Technology (HIT), Shenzhen, HIT Campus of University Town of Shenzhen, Shenzhen, 518055, China. E-mail: zhangling2018@hit.edu.cn
[c]Research Centre of Flexible Printed Electronic Technology, Harbin Institute of Technology, Shenzhen, 518055, China
[d]Zhuhai Institute of Advanced Technology Chinese Academy of Sciences, Zhuhai, 519000, China

† Electronic supplementary information (ESI) available. See DOI: 10.1039/c9ra03373d

capacity (1507 mA h g^{-1} at 0.2 A g^{-1}) as well as good capacity retention (1292 mA h g^{-1} after 45 cycles). Additionally, it showed a superior rate capacity when the current density was reduced to 0.2 A g^{-1} from 4.0 A g^{-1}, maintaining a rate capacity of 1375 mA h g^{-1}. Successfully, this hydrothermal method was applied for *in situ* growth of two more TMOs nanosheets standing on Ni foam, namely Fe_2O_3 and NiO. The same uniform structures and large surface area were obtained, confirming the universality and efficiency of this strategy.

Experimental

Materials

$Zn(NO_3)_2 \cdot 6H_2O$, $Ni(NO_3)_2 \cdot 6H_2O$, $Fe(NO_3)_2 \cdot 9H_2O$, NH_4F, $CO(NH_2)_2$ (urea) $(CH_2OH)_2$ (ethylene glycol), and ZnO powders were purchased from Shanghai Macklin Biochemical Co., Ltd (China). The electrolyte (1 M $LiPF_6$ in EC/DEC, 1 : 1 v/v), metallic Li, and Ni foam were purchased from Canrd Co., Ltd (China).

Treatment for Ni foam

Ni foam disks (*d*, 13 mm) were cut from the parent Ni foam (250 mm × 300 mm × 1 mm) using a sheet-punching machine. Further, Ni foam disks were treated with 3 M HCl solution for 10 min to remove the surface oxide layer and organic matter and rinsed with ethanol and deionized water, and dried thoroughly.

Synthesis of ZnO nanosheets@Ni foam

ZnO nanosheets@Ni foam was prepared by a facile hydrothermal reaction. In a typical synthesis procedure, 378 mg (2 mmol) $Zn(NO_3)_2 \cdot 6H_2O$, 480 mg (8 mmol) $CO(NH_2)_2$, and 222 mg (6 mmol) NH_4F were dissolved in 30 mL deionized water and 5 mL $(CH_2OH)_2$ to obtain a homogeneous solution. The pretreated Ni foam disks were placed in the solutions in Teflon-lined stainless-steel autoclaves. After 10 h at 120 °C, the samples were allowed to cool down to room temperature naturally and washed with deionized water, dried thoroughly, and annealed under air at 450 °C for 3 h at a heating rate of 1.5 °C min^{-1} to convert the intermediates to ZnO. The synthesis of Fe_2O_3 and NiO nanosheets@Ni foam was similar to that of ZnO nanosheets@Ni foam, except that Zn^{2+} precursors were replaced by Fe^{2+} and Ni^{2+} precursors.

Characterization

Field emission scanning electron microscopy (FESEM) images were obtained using a SEM HITACHI SU8010 (Japan). X-ray diffraction (XRD) patterns were obtained on Rigaku D/max diffractometer with Cu Kα radiation. X-ray photoelectron spectroscopy (XPS) data were collected on XPS PHI 5000 VersaProbe II instrument (USA). The Brunauer–Emmett–Teller (BET) surface area measurements were conducted using a Micromeritics ASAP 2020 HD88 (USA).

Electrochemical measurements

For battery tests, ZnO nanosheets@Ni foam disks (*d*, 13 mm) were used as anodes, which were loaded with ZnO nanosheets of 3–5 mg cm^{-2} (including 0.23 mg cm^{-2} NiO, experimental in ESI†). As a comparison, commercial ZnO powders were used to construct the anode. 75% ZnO, 15% Super P, and 10% polyvinylidene difluoride in *N*-methyl pyrrolidone solvent were mixed in to slurry, which were coated slurry onto copper foils (*d*, 13 mm) with 4–5 mg, which were dried in vacuum for 24 h. Electrochemical measurements were performed using coin cells (CR2032) with metallic Li (diameter, 16 mm) as the counter electrode, and 1 M $LiPF_6$ in ethylene carbonate and diethyl carbonate (EC/DEC, 1 : 1 v/v) as the electrolyte and separator. All the batteries were assembled in an argon glovebox with oxygen and water content lower than 0.1 ppm. The cycle life and rate capacity were evaluated using NEWARE battery testing systems (China) within the potential range of 0.01–3.0 V (*vs.* Li^+/Li) at room temperature. Cyclic voltammetry curves (CVs) were recorded at 0.1 mV s^{-1} in the potential window of 0.01–3.0 V on CORRTEST CS2350 electrochemical workstations (China). Electrochemical impedance spectroscopy (EIS) experiments were performed on CHI 760E electrochemical workstations (China) over a frequency range from 100 kHz to 0.01 Hz at open circuit voltages (2.7 ± 0.2 V).

Results and discussion

Synthesis and characterizations of ZnO nanosheets@Ni foam

The facile synthesis of ZnO nanosheets@Ni foam followed two steps. First, the precursor nanosheets were grown *in situ* on Ni foam *via* a simple hydrothermal method. Then, the intermediate products were converted to ZnO nanosheets by calcinations at 450 °C under air. As seen in Fig. S1 and S2,† good crystalline structures were obtained for intermediates, which were uniform nanosheets highly standing on Ni foam substrate. The intermediate product would be Zn^{2+} coordination complexes with F^-, $-NH_2$ or C=O as the ligands, which are similar to the structures of metal–organic framework.[39] The morphology of standing nanosheets on Ni foam was kept after calcinations (Fig. 1). The ZnO nanosheets had the thickness of approximate 50 nm, thus capable of increasing the reaction active areas exposed to electrolyte and providing efficient charge transportation pathways to obtain high specific capacities. Further, the relatively large voids between the two nanosheets buffer the volume change effectively, thus maintaining cyclability after lithiations.

N_2 adsorption–desorption isotherms and Barrett–Joyner–Halenda pore-size distribution curves were used for analysing

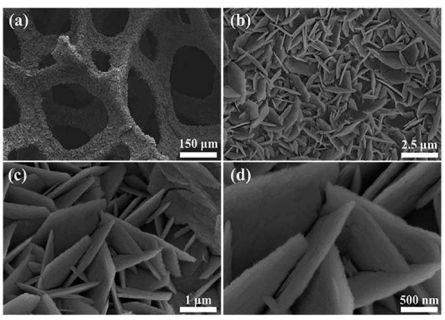

Fig. 1 SEM images of ZnO nanosheets@Ni foam at different magnifications.

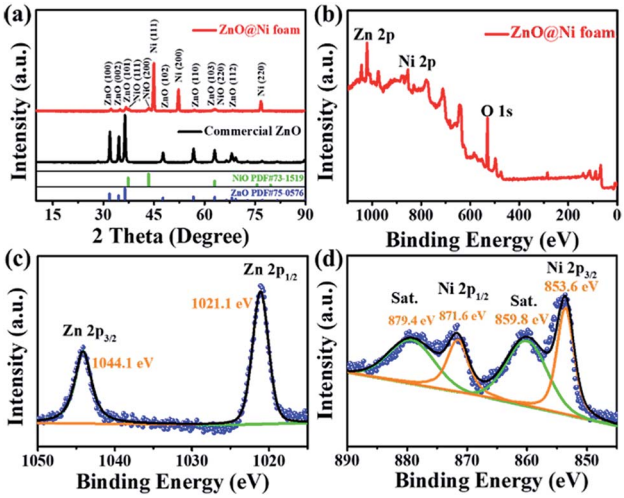

Fig. 2 (a) XRD patterns of ZnO nanosheets@Ni foam and commercial ZnO powders; (b–d) XPS patterns of ZnO nanosheets@Ni foam.

the specific surface area and porosity of ZnO nanosheets (Fig. S3†). The specific surface area of ZnO@Ni foam and commercial ZnO powder were measured to be 26.46 and 4.08 $m^2\ g^{-1}$, and the corresponding total pore volume were 0.11 and 0.01 $cm^3\ g^{-1}$, respectively. The pore sizes of ZnO nanosheets were mainly distributed around 70 nm, which was larger than that of commercial Zn powders (around 48 nm).

XRD patterns (Fig. 2a) for ZnO nanosheets@Ni foam and commercial ZnO powder exhibited peaks at 31.8°, 34.5°, 36.3°, 47.6°, 56.7°, 63.0°, and 68.1°, corresponding to the (100), (002), (101), (102), (110), (103), and (112) planes of hexagonal phase of ZnO crystals, respectively (ICSD no. 75-0576). Three peaks were assigned to the Ni foam substrate at 44.9°, 52.2°, and 76.8°, corresponding to the (111), (200), and (220) planes of cubic phase of Ni foam, respectively (ICSD no. 70-1849). Two peaks at 37.1° and 43.4° were assigned to (111) and (200) plane of NiO, which formed after calcinations taking for 1.0% in weight of total mass of Ni and NiO (Fig. S4†).

XPS measurement of ZnO nanosheets@Ni foam was performed in order to assess the chemical states of elements (Fig. 2b). Zn $2p_{3/2}$ and $2p_{1/2}$ peaks were found at 1044.1 and 1021.1 eV, respectively, corresponding to Zn(II) of ZnO nanosheets (Fig. 2c). Ni $2p_{3/2}$ and $2p_{1/2}$ XPS peaks at 853.6 and 871.6 eV along with their satellite peaks at 859.8 and 879.4 eV were observed, respectively, corresponding to the metallic Ni foam substrate[31,36] (Fig. 2d). Based on the XRD and XPS analysis, it was concluded that ZnO nanosheets crystalline were successfully grown *in situ* on the Ni foam.

Electrochemical performance of ZnO nanosheets@Ni foam

The electrochemical performance of the ZnO nanosheets@Ni foam electrodes was assessed through charge/discharge voltage profiles and CVs (Fig. 3). The cathodic peak in the first scan at 0.43 V covered the multi-step reactions, including the reductions of ZnO, the formations of solid electrolyte interface (SEI)[11,23,40] and $LiZn_xNi_y (y \ll x \leq 1)$ alloy (eqn (1) and (2)) (Fig. 3a). Trace of Ni elements is alloyed, and the reduction peak of NiO locate around 1.4 V in the first cathodic scan and 1.7 V (a few) in the following scans, which was further demonstrated by CVs of commercial ZnO particles on Cu foil (Fig. S5†). In the first anodic scan, the corresponding dealloying reactions of $LiZn_xNi_y (y \ll x \leq 1)$, the oxidations of Zn to ZnO and Ni to NiO occur around 1.0, 1.7 and 2.3 (both for ZnO and NiO) V,

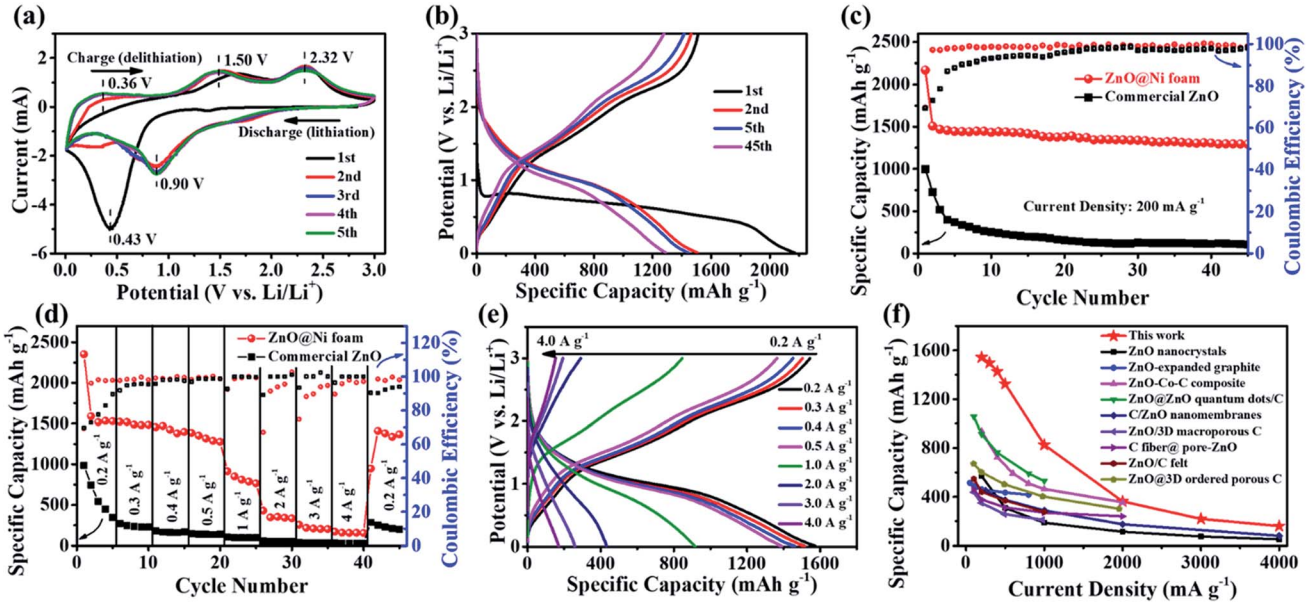

Fig. 3 Electrochemical performance of tested materials. (a) CVs at 0.1 mV s^{-1} and (b) galvanostatic charge–discharge curves at 0.2 A g^{-1} of ZnO nanosheets@Ni foam at different cycles; (c) cycling performance at 0.2 A g^{-1} and (d) rate performance at various current densities of ZnO nanosheets@Ni foam and commercial ZnO@Cu foil; (e) galvanostatic charge–discharge curves at various current density; (f) comparisons of the rate performance of ZnO nanosheets@Ni foam in this work with those of ZnO nanomaterials-based anodes reported by previous studies.[23,39–50]

respectively, which shift negatively in the following anodic scans and the reactions become stable after 4 cycles (eqn (3) and (4)) (Fig. 3a). The reductions of NiO, ZnO and the alloy process occur around 1.7 (both for ZnO and NiO), 0.9, and 0.6 V, respectively after 4 cycles.[21,23,31,41–43]

$$x\mathrm{ZnO} + y\mathrm{NiO} + 2(x+y)\mathrm{e} \rightarrow \mathrm{Zn}_x\mathrm{Ni}_y \text{ (1.7 and 0.9 V)} \quad (1)$$

$$\mathrm{Zn}_x\mathrm{Ni}_y + \mathrm{Li}^+ + \mathrm{e} \rightarrow \mathrm{LiZn}_x\mathrm{Ni}_y \text{ (0–0.6 V)} \quad (2)$$

$$\mathrm{LiZn}_x\mathrm{Ni}_y - \mathrm{e} \rightarrow \mathrm{Li} + \mathrm{Zn}_x\mathrm{Ni}_y \text{ (0–0.6 V)} \quad (3)$$

$$\mathrm{Zn}_x\mathrm{Ni}_y - 2(x+y)\mathrm{e} \rightarrow x\mathrm{ZnO} + y\mathrm{NiO} \text{ (1.5 and 2.3 V)} \quad (y \ll x \leq 1) \quad (4)$$

The representative charge/discharge voltage profiles of ZnO nanosheets@Ni foam between 0.01 and 3.0 V (*vs.* Li/Li^+) at a current rate of 0.2 A g^{-1} also demonstrated the delithiation and lithiation reactions. The voltage plateaus in the first and subsequent cycles were in good agreement with the anodic and cathodic peak positions observed in CVs (Fig. 3b). Following the initial capacity loss which contributes to the formation of the SEI film, ZnO nanosheets@Ni foam delivered a reversible capacity of 1507 mA h g^{-1} (5.45 mA h cm^{-2}, Fig. S6†) for the first charge process and maintained a stable capacity of 1292 mA h g^{-1} at the 45th cycle.

The cycling stability performance of ZnO nanosheets@Ni foam under the current density of 0.2 A g^{-1} was compared with that of commercial ZnO@Cu foil under the same conditions (Fig. 3c). ZnO nanosheets@Ni foam exhibited a high capacity and retention of 85.7%, along with a nearly 100% coulombic efficiency after 45 cycles. The high capacity and good retention values should be attributed to the formation of LiO as well as $LiZn_xNi_y(y \ll x \leq 1)$ alloy and interfacial lithium storage.[31,51,52] The extra capacity that offered by theoretical value is ascribed to interfacial lithium ion storages mechanism, which is due to ZnO@Ni foam electrode's special structure (large surface area, pore size and pore volume) and good conductivity to provide more active sites to store interfacial lithium ion. These results were in obvious contrast to those of commercial ZnO electrode, where the capacity underwent fast fading from 996 mA h g^{-1} to 106 mA h g^{-1} after 45 cycles with the capacity retention of 14.6%. The poor electrochemical performance was probably caused by the aggregations of ZnO particles (Fig. S7†), and a part of ZnO cannot participate in the alloying reactions. The low capacity retention was mainly due to the volume change by the exfoliations of active materials.

The rate performance of ZnO nanosheets@Ni foam was investigated by charging and discharging at various current rates within the range of 0.2 to 4.0 A g^{-1} (Fig. 3d and e). The electrodes were able to deliver average reversible specific capacities of 1542, 1498, 1427, 1325, 826, 362, 219 and 158 mA h g^{-1} at the current densities of 0.2, 0.3, 0.4, 0.5, 1.0, 2.0, 3.0 and 4.0 A g^{-1}, respectively. Even under the high current density of 4.0 A g^{-1}, ZnO nanosheets@Ni foam still retained a high specific capacity of 158 mA h g^{-1} after 45 cycles. When the current density returned to 0.2 A g^{-1}, a reversible capacity of 1375 mA h g^{-1} was recorded, revealing the good cycling reversibility. In sharp contrast, the discharge capacity of the commercial ZnO@Cu foil faded fast as the current rate increased and the capacity dropped to almost zero at the high current density from 2.0 to 4.0 A g^{-1} (Fig. 3d). The results demonstrated the good cycling stability of ZnO nanosheets@Ni foam electrode. Compared with the previously reported ZnO nanomaterials-based anode in LIBs, ZnO nanosheets@Ni foam prepared in this work exhibited better electrochemical performance with regards to rate capacity and specific capacity, which should be attributed to the standing ZnO nanosheet structures and binder free to conductive Ni foam (Fig. 3f).[23,39–50]

EIS measurements were performed to further explore the electrochemical properties of the prepared materials. The Nyquist plots are composed of a semicircle corresponding to charge-transfer resistance (R_{ct}) at high frequency region and an inclined line at the low frequency region.[53,54] R_{ct} of ZnO nanosheets@Ni foam was much lower than that of the commercial ZnO@Cu foil, confirming that the charge transfer on ZnO nanosheets@Ni foam occurs rapidly (Fig. 4a). It was attributed to the Ni foam skeleton with porous structures being an excellent conductor as well as the nanosheet structures of ZnO, which possessed large surface areas enabling the rapid Li^+ diffusions compared to the commercial ZnO powders. EIS spectra at various cycles were carried out with one cell after charging to 3 V for different cycling (Fig. 4b).

After the initial cycle, R_{ct} increased rapidly due to the formation of SEI film hindering the transportation of Li^+ (Fig. 4b). As the cycle progressed, R_{ct} increased slowly and was stabilized gradually after 20 cycles with a relatively low resistance.

Ex situ characterizations of Zn nanosheets@Ni foam structures in charge/discharge process

In order to explore the underlying electrochemical reaction mechanism inducing the excellent battery performance of ZnO nanosheets@Ni foam, the crystal phase, structure, and morphology were monitored *ex situ* by XRD, XPS, and SEM measurements in the discharge and charge process. XRD patterns of ZnO nanosheets@sheets exhibited good reversibility as the same as those of the specific capacity at different potentials (Fig. 5). During lithiation (from pristine discharge to different potential at 1.5, 0.6, and 0.01 V), the XRD peaks of ZnO

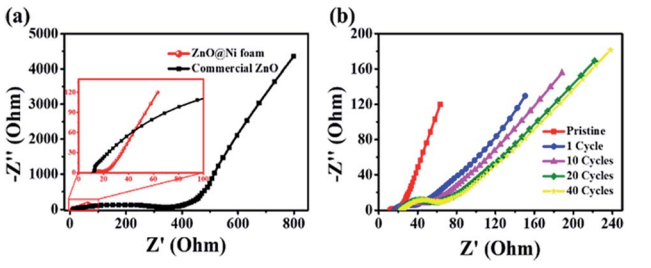

Fig. 4 Nyquist plots for EIS analysis of (a) ZnO@Ni foam and commercial ZnO and (b) ZnO@Ni foam after various cycles.

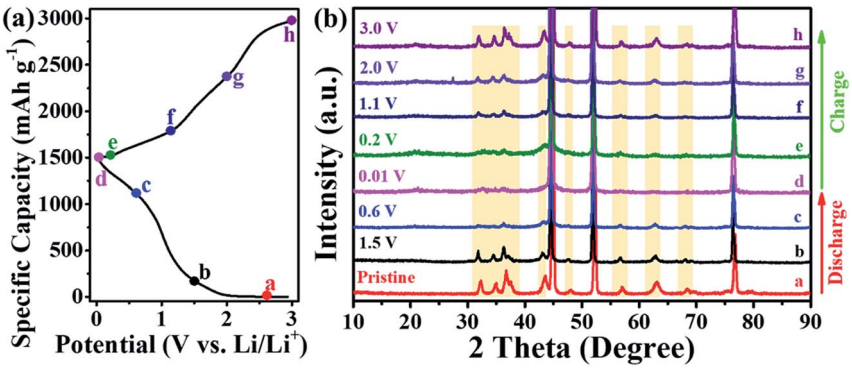

Fig. 5 (a) Specific capacities and (b) *ex situ* XRD patterns of Zn nanosheets@Ni foam in discharge and charge processes of LIBs.

nanosheets@Ni foam electrode for ZnO and NiO phase decreased gradually and eventually disappeared (Fig. 5b, curve a to d), demonstrating the consumption of ZnO during lithiation (eqn (1) and (2)). Upon charging from 0.01 V to 0.2, 1.1, 2.0, and 3.0 V, XRD peaks for ZnO and NiO were recovered, thus indicating good reversibility of ZnO nanosheets@Ni foam (Fig. 5b, curve d to h).

Ex situ XPS and SEM characterizations provided detailed information on the structures of ZnO nanosheets@Ni foam during lithiation and delithiation (Fig. 6). Similar changes in the XPS signals for Zn $2p_{3/2}$ (1044.1 eV) and $2p_{1/2}$ (1021.1 eV) peaks, which diminished and vanished in the discharging process for the formations of $LiZn_xNi_y (y \ll x \leq 1)$ alloy (eqn (1) and (2)) and recovered in the charging process for the formations of ZnO (eqn (3) and (4), Fig. 6a and b). More importantly, the state changes of O_{1s} were observed obviously during the reactions. In the discharging reactions, the signals for O_{1s} of Zn–O bond (529.5 eV) and Ni–O bond (531.2

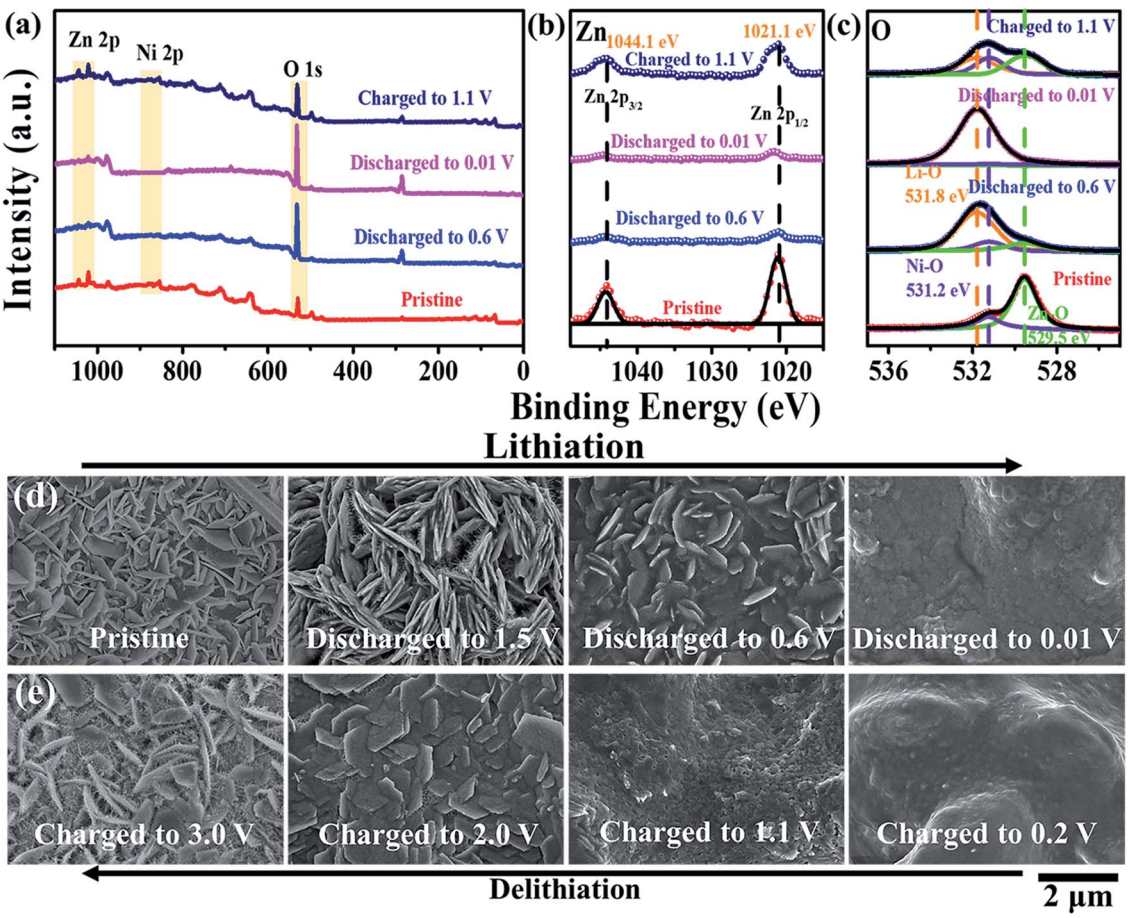

Fig. 6 *Ex situ* (a–c) XPS data and (d and e) SEM images of Zn nanosheets@Ni foam in discharge and charge processes of LIBs.

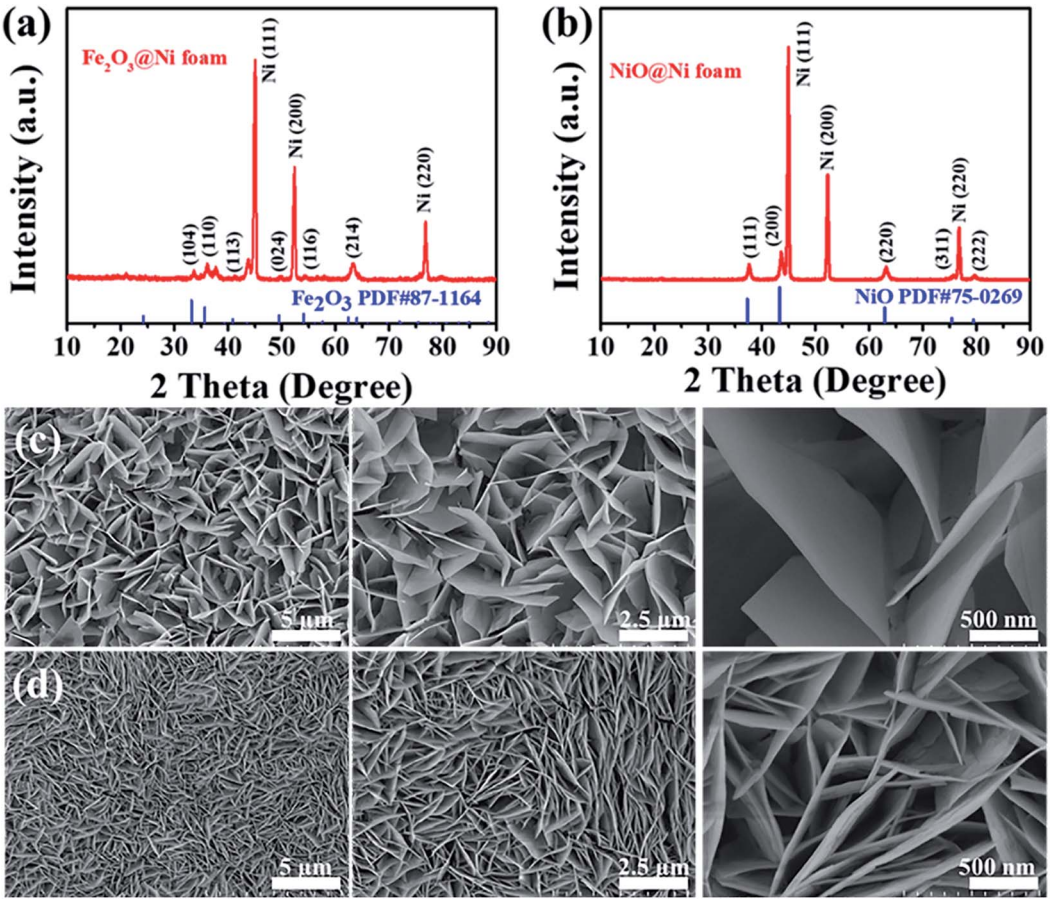

Fig. 7 (a and b) XRD patterns and (c and d) SEM images of Fe_2O_3 nanosheets (a and c) and NiO nanosheets (b and d) *in situ* grown on Ni foam.

eV) diminished and disappeared completely at 0.01 V (Fig. 6c). On the contrary, the signals for O_{1s} of Li–O bond (531.8 eV) appeared and increased distinctly, providing evidence for the formation of Li_2O and $LiZn_xNi_y (y \ll x \leq 1)$ alloy in the discharging process (eqn (1) and (2)). When the potential was back to 1.1 V in the charging process, the signals of O_{1s} for Zn–O, Ni–O, and Li–O bond recovered to the former values, respectively, confirming the reversible lithiation and delithiation processes of ZnO nanosheets@Ni foam.

The morphology of ZnO nanosheet@Ni foam provided us the evident information about the reactions. Three cells for every process (total 24 cells) were used to investigate the changes in morphology for every potential (experimental in ESI†). As shown in Fig. 6d, the structures of the electrode were changed and the blurry surface was formed in the discharge process. As we note, the needle-shaped crystals were grown on the nanosheets at 1.5 V, suggesting the formation process of $LiZn_xNi_y (y \ll x \leq 1)$ alloy. When the potential was increased to 0.2, 1.1, 2.0, and 3.0 V in the charging process, the electrode surface recovered to the former state, demonstrating the stability of the ZnO nanosheets@Ni foam (Fig. 6e).

Finally, the hydrothermal *in situ* growth method was extended to synthesize Fe_2O_3 and NiO nanosheets on Ni foam successfully. Both of the two TMO nanosheets were formed on Ni foam with good crystalline and uniform morphology (Fig. 7). It is expected that the good electrochemical performance of Fe_2O_3 and NiO nanosheets on Ni foam are exhibited in the applications of LIBs and other electronic devices.

Conclusions

The work presents a facile hydrothermal method for *in situ* growth of ZnO nanosheets on Ni foam applied as a high-performance LIB anode. The obtained structures have several advantages, (1) uniform nanosheet structures standing on Ni foam provide large surface areas and highly efficient charge transportation pathway; (2) large voids between the two adjacent nanosheets buffer the volume changes during lithiation/delithiation process; (3) the use of conductor, Ni foam framework as substrate to grow the binder-free Zn nanosheets directly decreases the interface resistance and increases the electrode conductivity dramatically. The advantages of the structures make ZnO nanosheets@Ni foam possess high specific capacity and excellent rate performance, which are superior to other ZnO based nanomaterials reported in previous literatures. The synthetic strategy is universal, effective and economic for constructing good binder-free anodes applied in LIBs practically.

Conflicts of interest

There are no conflicts to declare.

Acknowledgements

This work was supported by the National Natural Science Foundation of China (21703218), the Shenzhen Science and Technology Innovation Committee (JCYJ20151013162733704), Economic, Trade and Information Commission of Shenzhen Municipality through the Graphene Manufacture Innovation Center [201901161514] and the Thousand Talents Plan (Youth).

References

1 M. Armand and J. M. Tarascon, *Nature*, 2008, **451**, 652–657.
2 B. Dunn, H. Kamath and J. M. Tarascon, *Science*, 2011, **334**, 928–935.
3 J. B. Goodenough, *Acc. Chem. Res.*, 2013, **46**, 1053–1061.
4 M. Li, J. Lu, Z. Chen and K. Amine, *Adv. Mater.*, 2018, **30**, 1800561.
5 D. Lin, Y. Liu and Y. Cui, *Nat. Nanotechnol.*, 2017, **12**, 194–206.
6 N. Nitta, F. Wu, J. T. Lee and G. Yushin, *Mater. Today*, 2015, **18**, 252–264.
7 W.-J. Zhang, *J. Power Sources*, 2011, **196**, 13–24.
8 Y. Zhao, X. Li, B. Yan, D. Xiong, D. Li, S. Lawes and X. Sun, *Adv. Energy Mater.*, 2016, **6**, 1502175.
9 A. Magasinski, P. Dixon, B. Hertzberg, A. Kvit, J. Ayala and G. Yushin, *Nat. Mater.*, 2010, **9**, 353–358.
10 G. Zhou, D.-W. Wang, F. Li, L. Zhang, N. Li, Z.-S. Wu, L. Wen, G. Q. Lu and H.-M. Cheng, *Chem. Mater.*, 2010, **22**, 5306–5313.
11 S. Zhu, J. Li, X. Deng, C. He, E. Liu, F. He, C. Shi and N. Zhao, *Adv. Funct. Mater.*, 2017, **27**, 1605017.
12 A. B. Djurišić, A. M. C. Ng and X. Y. Chen, *Prog. Quantum Electron.*, 2010, **34**, 191–259.
13 A. Gaiardo, B. Fabbri, A. Giberti, V. Guidi, P. Bellutti, C. Malagù, M. Valt, G. Pepponi, S. Gherardi, G. Zonta, A. Martucci, M. Sturaro and N. Landini, *Sens. Actuators, B*, 2016, **237**, 1085–1094.
14 J. Guo, J. Zhang, M. Zhu, D. Ju, H. Xu and B. Cao, *Sens. Actuators, B*, 2014, **199**, 339–345.
15 F.-X. Liang, Y. Gao, C. Xie, X.-W. Tong, Z.-J. Li and L.-B. Luo, *J. Mater. Chem. C*, 2018, **6**, 3815–3833.
16 H. Wang, W. Lin, X. Qiu, F. Fu, R. Zhong, W. Liu and D. Yang, *ACS Sustainable Chem. Eng.*, 2018, **6**, 3696–3705.
17 K. Zhang, Z. L. Wang and Y. Yang, *ACS Nano*, 2016, **10**, 10331–10338.
18 Q. Zhang, C. S. Dandeneau, X. Zhou and G. Cao, *Adv. Mater.*, 2009, **21**, 4087–4108.
19 Y. C. Chen, C. H. Lin, T. F. Guo and T. C. Wen, *ACS Appl. Mater. Interfaces*, 2018, **10**, 26805–26811.
20 G. Wu, Z. Jia, Y. Cheng, H. Zhang, X. Zhou and H. Wu, *Appl. Surf. Sci.*, 2019, **464**, 472–478.
21 X. H. Huang, R. Q. Guo, J. B. Wu and P. Zhang, *Mater. Lett.*, 2014, **122**, 82–85.
22 S. Wi, H. Woo, S. Lee, J. Kang, J. Kim, S. An, C. Kim, S. Nam, C. Kim and B. Park, *Nanoscale Res. Lett.*, 2015, **10**, 204.
23 W. Zhang, L. Du, Z. Chen, J. Hong and L. Yue, *J. Nanomater.*, 2016, **2016**, 1–7.
24 A. Kushima, X. H. Liu, G. Zhu, Z. L. Wang, J. Y. Huang and J. Li, *Nano Lett.*, 2011, **11**, 4535–4541.
25 Y. Zhang, Z. Wang, Y. Li and K. Zhao, *Mech. Mater.*, 2015, **91**, 313–322.
26 R. Guo, W. Yue, Y. An, Y. Ren and X. Yan, *Electrochim. Acta*, 2014, **135**, 161–167.
27 L. Xiao, E. Li, J. Yi, W. Meng, S. Wang, B. Deng and J. Liu, *J. Alloys Compd.*, 2018, **764**, 545–554.
28 R. Yang, H. Du, Z. Lin, L. Yang, H. Zhu, H. Zhang, Z. Tang and X. Gui, *Carbon*, 2019, **141**, 258–265.
29 Z. Ren, Z. Wang, C. Chen, J. Wang, X. Fu, C. Fan and G. Qian, *Electrochim. Acta*, 2014, **146**, 52–59.
30 B. N. Joshi, S. An, H. S. Jo, K. Y. Song, H. G. Park, S. Hwang, S. S. Al-Deyab, W. Y. Yoon and S. S. Yoon, *ACS Appl. Mater. Interfaces*, 2016, **8**, 9446–9453.
31 N. Li, S. X. Jin, Q. Y. Liao and C. X. Wang, *ACS Appl. Mater. Interfaces*, 2014, **6**, 20590–20596.
32 B. Oschmann, M. N. Tahir, F. Mueller, D. Bresser, I. Lieberwirth, W. Tremel, S. Passerini and R. Zentel, *Macromol. Rapid Commun.*, 2015, **36**, 1075–1082.
33 H. Tan, H.-W. Cho and J.-J. Wu, *J. Power Sources*, 2018, **388**, 11–18.
34 D. Wang, J. Guo, C. Cui, J. Ma and A. Cao, *Mater. Res. Bull.*, 2018, **101**, 305–310.
35 Y. Wang, S. Fan, F. Liao, X. Zheng, Z. Huang, Y. Wang and X. Han, *Nanoscale Adv.*, 2019, **1**, 1200–1206.
36 S. Lu, H. Wang, J. Zhou, X. Wu and W. Qin, *Nanoscale*, 2017, **9**, 1184–1192.
37 H. Ning, H. Xie, Q. Zhao, J. Liu, W. Tian, Y. Wang and M. Wu, *J. Alloys Compd.*, 2017, **722**, 716–720.
38 J. Yuan, X. Zhang, C. Chen, Y. Hao, R. Agrawal, C. Wang, W. Li, H. Yu, Y. Yu, X. Zhu, Z. Xiong and Y. Xie, *Mater. Lett.*, 2017, **190**, 37–39.
39 M. Eddaoudi, J. Kim, N. Rosi, D. Vodak, J. Wachter, M. O'Keeffe and O. M. Yaghi, *Science*, 2002, **295**, 469–472.
40 C. Zhang, Z. Zhang, F. Yin, Y. Zhang, A. Mentbayeva, M.-R. Babaa, A. Molkenova and Z. Bakenov, *ChemElectroChem*, 2017, **4**, 2359–2365.
41 Y. Teng, M. Mo, Y. Li, J. Xue and H. Zhao, *J. Alloys Compd.*, 2018, **744**, 712–720.
42 Y. Teng, H. Zhao, Z. Zhang, Y. Li and H. Liu, *Mater. Lett.*, 2019, **246**, 141–143.
43 X. H. Huang, X. H. Xia, Y. F. Yuan and F. Zhou, *Electrochim. Acta*, 2011, **56**, 4960–4965.
44 Y. Li, Y. Zhao, G. Huang, B. Xu, B. Wang, R. Pan, C. Men and Y. Mei, *ACS Appl. Mater. Interfaces*, 2017, **9**, 38522–38529.
45 X. Lu, A. Xie, C. Jiang, M. Lu, Y. Zhang, H. Zhong and S. Zhuang, *RSC Adv.*, 2017, **7**, 4269–4277.
46 G. Zhang, S. Hou, H. Zhang, W. Zeng, F. Yan, C. C. Li and H. Duan, *Adv. Mater.*, 2015, **27**, 2400–2405.
47 Y. Zhao, G. Huang, Y. Li, R. Edy, P. Gao, H. Tang, Z. Bao and Y. Mei, *J. Mater. Chem. A*, 2018, **6**, 7227–7235.

48 Q. Han, X. Li, F. Wang, Z. Han, D. Geng, W. Zhang, Y. Li, Y. Deng, J. Zhang, S. Niu and L. Wang, *J. Electroanal. Chem.*, 2019, **833**, 39–46.
49 X. Shen, Z. Cao, J. Zhang, T. Li and W. Jiang, *Mater. Lett.*, 2018, **229**, 93–97.
50 F. Yin, Z. Zhang, Y. Zhang, C. Zhang and L. Xu, *Electrochim. Acta*, 2018, **270**, 274–283.
51 J. Wang, N. Yang, H. Tang, Z. Dong, Q. Jin, M. Yang, D. Kisailus, H. Zhao, Z. Tang and D. Wang, *Angew. Chem., Int. Ed.*, 2013, **52**, 6417–6420.
52 J. Maier, *Nat. Mater.*, 2005, **4**, 805–815.
53 S.-D. Xu, Q.-C. Zhuang, L.-L. Tian, Y.-P. Qin, L. Fang and S.-G. Sun, *J. Phys. Chem. C*, 2011, **115**, 9210–9219.
54 G. Du and F. L. Mantia, *ChemElectroChem*, 2017, **4**, 122–129.